ACS NANO
Cite This: ACS Nano 2018, 12, 2968–2979
www.acsnano.org

ARTICLE

In Situ Growth of Layered Bimetallic ZnCo Hydroxide Nanosheets for High-Performance All-Solid-State Pseudocapacitor

Zhichang Pan,[†] Yingchang Jiang,[†] Peiyu Yang,[†] Zeyi Wu,[†] Wenchao Tian,[†] Liu Liu,[†] Yun Song,[†] Qinfen Gu,[*,‡] Dalin Sun,[*,†] and Linfeng Hu[*,†]

[†]Department of Materials Science, Fudan University, Shanghai 200433, P.R. China
[‡]Australia Synchrotron (ANSTO), 800 Blackburn Road, Clayton 3168, Australia

Supporting Information

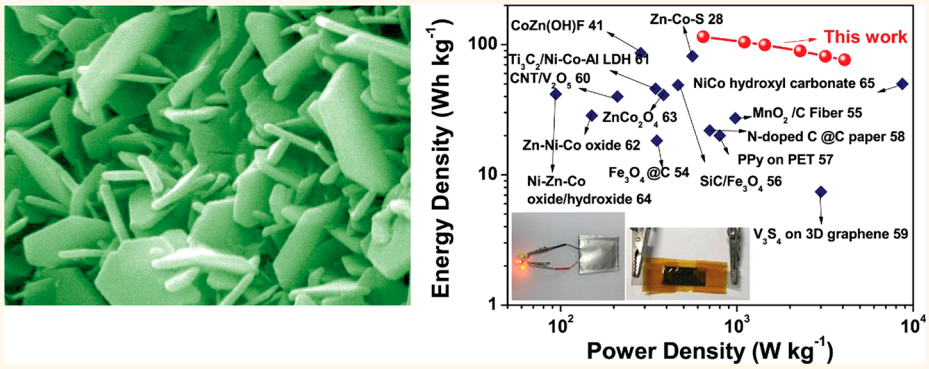

ABSTRACT: Two-dimensional (2D) hydroxide nanosheets can exhibit exceptional electrochemical performance owing to their shortened ion diffusion distances, abundant active sites, and various valence states. Herein, we report $ZnCo_{1.5}(OH)_{4.5}Cl_{0.5}{\cdot}0.45H_2O$ nanosheets (thickness ~30 nm) which crystallize in a layered structure and exhibit a high specific capacitance of 3946.5 F g^{-1} at 3 A g^{-1} for an electrochemical pseudocapacitor. $ZnCo_{1.5}(OH)_{4.5}Cl_{0.5}{\cdot}0.45H_2O$ was synthesized by a homogeneous precipitation method and spontaneously crystallized into 2D nanosheets in well-defined hexagonal morphology with crystal structure revealed by synchrotron X-ray powder diffraction data analysis. *In situ* growth of $ZnCo_{1.5}(OH)_{4.5}Cl_{0.5}{\cdot}0.45H_2O$ nanosheet arrays on conductive Ni foam substrate was successfully realized. Asymmetric supercapacitors based on $ZnCo_{1.5}(OH)_{4.5}Cl_{0.5}{\cdot}0.45H_2O$ nanosheets @Ni foam// PVA, KOH//reduced graphene oxide exhibits a high energy density of 114.8 Wh kg^{-1} at an average power density of 643.8 W kg^{-1}, which surpasses most of the reported all-solid-state supercapacitors based on carbonaceous materials, transition metal oxides/hydroxides, and MXenes. Furthermore, a supercapacitor constructed from $ZnCo_{1.5}(OH)_{4.5}Cl_{0.5}{\cdot}0.45H_2O$ nanosheets@PET substrate shows excellent flexibility and mechanical stability. This study provides layered bimetallic hydroxide nanosheets as promising electroactive materials for flexible, solid-state energy storage devices, presenting the best reported performance to date.

KEYWORDS: *$ZnCo_{1.5}(OH)_{4.5}Cl_{0.5}{\cdot}0.45H_2O$ nanosheets, crystal structure solvation, in situ growth, specific capacitance, solid-state supercapacitors*

The emergence of high-efficiency energy storage devices has attracted widespread interests due to the ever-increasing demands for renewable energy. Electrochemical pseudocapacitors, also known as supercapacitors, are promising energy storage devices for modern electronics due to their excellent features, including ultra-high-power density, fast charge−discharge rate, environmental friendliness, and long cycling life.[1−3] However, the practical applications of supercapacitors in electric vehicles and portable electronics are still hindered due to the lack of high-performance electrode materials at a reasonable cost. In the past decades, various electrode materials, including carbonaceous materials, conducting polymers, and transition metal oxides, have been widely developed to obtain superior performance. Nevertheless, carbonaceous materials generally suffer from a poor energy density that cannot meet the demands of modern electronics.[4] Conducting polymers suffer from poor cycling performance during long-term charge/discharge, leading to a poor cycling

Received: January 25, 2018
Accepted: February 22, 2018
Published: February 22, 2018

DOI: 10.1021/acsnano.8b00653
ACS Nano 2018, 12, 2968–2979

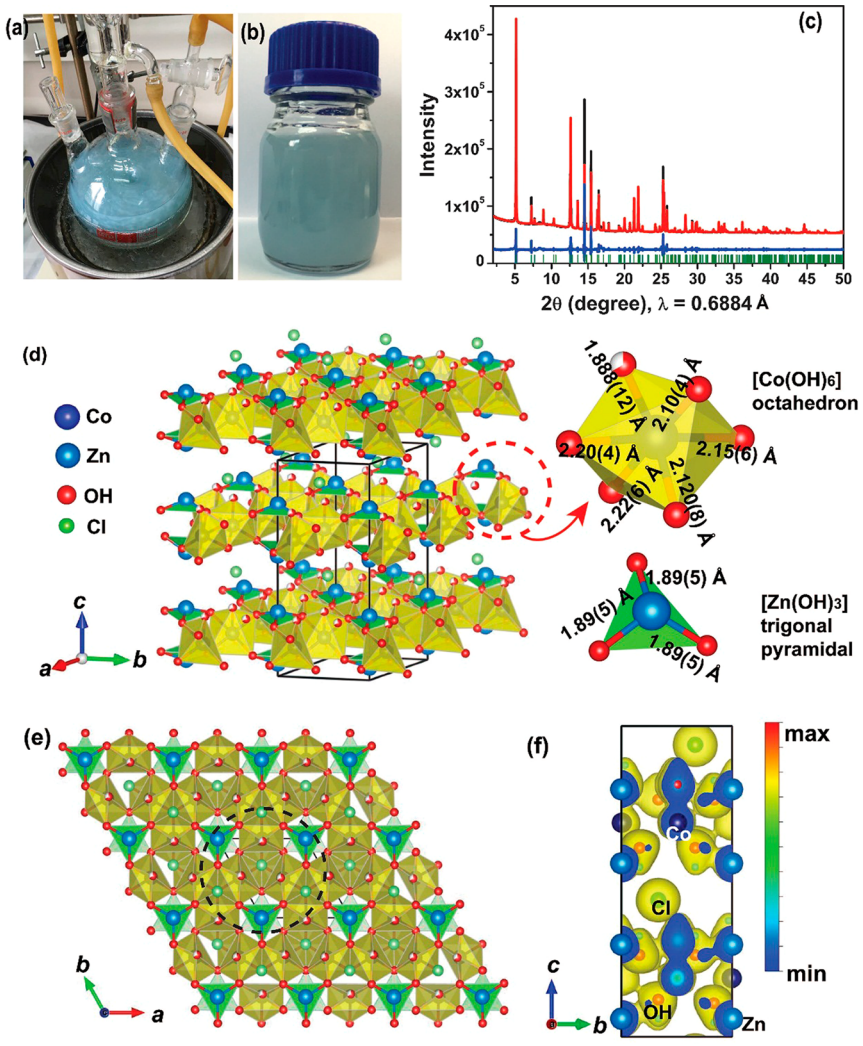

Figure 1. (a,b) Optical photographs of the synthesis process and the aqueous dispersion of $ZnCo_{1.5}(OH)_{4.5}Cl_{0.5}{\cdot}0.45H_2O$ sample. (c) Rietveld refinement of synchrotron X-ray powder diffraction of the $ZnCo_{1.5}(OH)_{4.5}Cl_{0.5}{\cdot}0.45H_2O$ powder. Red points correspond to the data points, and the black line denotes the calculated pattern. The difference is shown by the blue line. Calculated positions of Bragg reflections are marked by dark green vertical ticks. (d) 3D atomic configuration of a $ZnCo_{1.5}(OH)_{4.5}Cl_{0.5}{\cdot}0.45H_2O$ unit cell and the local coordination of strongly distorted $[Co(OH)_6]$ octahedra and $[Zn(OH)_3]$ trigonal pyramidal from synchrotron X-ray powder diffraction data. H atoms and water molecules are not shown for simplified view. (e) Atomic configuration of (001) crystal plane of the $ZnCo_{1.5}(OH)_{4.5}Cl_{0.5}{\cdot}0.45H_2O$ crystal. (f) Side view along the *a*-axis of the electron-density distribution obtained from electron-density distribution analysis by first-principles calculations.

life for supercapacitors.[5,6] On the other hand, low electrical conductivity and unsatisfactory rate capability of the transition metal oxides limit them from wide ranging commercialization.[7] Thus, the development and synthesis of new materials with high energy density, low cost, and long cycling life remains a challenging task for various energy storage devices.[8]

Recently, inorganic layered hydroxides with two-dimensional (2D) nanosheet morphology have attracted considerable interest in electrochemical properties and energy applications.[9−11] Typically, hydrotalcite-like cobalt, nickel hydroxide usually displays a positively charged layer and an interlayered gallery with negatively charged anions (*e.g.*, CO_3^{2-}, NO_3^-, Cl^-, *etc.*).[12,13] Several recent studies have focused on developing layered hydroxide electrodes that possess richer Faradaic reactions and higher capacities due to an improvement in pseudocapacitive properties. For example, Cheng *et al.* reported that an ultrathin α-$Co(OH)_2$ nanosheet electrode exhibited a specific capacitance of 833.4 F g^{-1} at 5 A g^{-1}.[14] Dai *et al.* rationally designed $Ni(OH)_2$ nanocrystals grown on graphene nanosheets, which exhibit a high specific capacitance of ∼1335 F/g at a charge and discharge current density of 2.8 A g^{-1} with excellent cycling ability.[15,16]

It has been well-established that bimetallic hydroxides generally show higher electrochemical activity than unitary hydroxides, owing to the complex composition and synergistic effects of multiple metal species.[17] Bimetallic layered double hydroxides (LDHs) with a general formula of $[M^{2+}_{1-x}M^{3+}_x(OH)_2]^{x+}$ $[A^{n-}_{x/n}{\cdot}mH_2O]_{x-}$ (M^{2+} and M^{3+}, the bivalent and trivalent metal cations, respectively; A^{n-}, the charge-balancing anion of valence *n*; $x = M^{3+}/(M^{2+} + M^{3+})$) are important members of the 2D inorganic family.[18−23] The great majority of layered hydroxides reported so far are generally Brucite or hydrotalcite structured compounds.[21−23] By appropriately adjusting anionic species, lamellar LDHs can generate attractive properties on energy storage arising from the ultimate 2D anisotropy and accessible high surface area, as

DOI: 10.1021/acsnano.8b00653
ACS Nano 2018, 12, 2968−2979

well as a peculiar positively charged feature.[24−26] Considering the high abundance of Zn resources,[27] outstanding Faradaic pesoducapacitive performance, and rich redox reactions of Zn−Co compounds,[28,29] bimetallic Zn−Co hydroxides should be very promising for future use in supercapacitors, and the rational synthesis of Zn−Co hydroxides with anisotropic 2D morphology is highly desired. However, although the catalysis and oxygen evolution reaction properties of Zn−Co LDHs have been widely reported,[30,31] very little attention has been paid to developing this material series on supercapacitor electrodes until now. Only Hwang *et al.* studied the exfoliation behavior of Zn−Co LDHs and revealed the pseudocapacitive properties of the Zn−Co−LDH film fabricated with the restacked Zn−Co LDH nanosheets after exfoliation.[32] This thin-film-based electrode exhibited pseudocapacitive behavior with a specific capacitance of 160−170 F g^{-1} at 1 A g^{-1} and a capacitance retention up to 50 cycles.

Our previous work has realized a facile *in situ* growth of Ni−Co and Ni−Fe LDH nanosheet arrays on a conductive matrix through a homogeneous precipitation process, displaying a high energy density (77.3 Wh kg^{-1} at 623 W kg^{-1} for Ni−Co LDH and 82.3 Wh kg^{-1} at 661 W kg^{-1} for Ni−Fe LDHs, respectively).[33,34] It is a logical consideration to prepare Zn−Co LDH nanosheet arrays using this strategy. Unexpectedly, we synthesized layered $ZnCo_{1.5}(OH)_{4.5}Cl_{0.5}{\cdot}0.45H_2O$ rather than the conventional Zn−Co LDH phase. We successfully solved its structure by synchrotron X-ray powder diffraction data analysis. The *in situ* growth of dense arrays of $ZnCo_{1.5}(OH)_{4.5}Cl_{0.5}{\cdot}0.45H_2O$ nanosheets (thickness ∼30 nm) on Ni foam endows a high specific capacitance of 3946.5 F g^{-1} at 3 A g^{-1}. The $ZnCo_{1.5}(OH)_{4.5}Cl_{0.5}{\cdot}0.45\ H_2O$ nanosheets@Ni foam//PVA, KOH//reduced graphene oxide (rGO) asymmetric supercapacitors exhibit a high energy density of 114.8 Wh kg^{-1} at an average power density of 643.8 W kg^{-1}. This value surpasses that of most recently reported all-solid-state supercapacitors based on carbonaceous materials, transition metal oxides/hydroxides, and MXenes. Taking advantage of their ultrathin nature and well-defined 2D morphology, a supercapacitor constructed from $ZnCo_{1.5}(OH)_{4.5}Cl_{0.5}{\cdot}0.45H_2O$ nanosheets@PET substrate shows excellent flexibility and mechanical stability for wearable and foldable devices. Our study provides layered Zn−Co bimetallic hydroxide nanosheets as promising electroactive materials for flexible, solid-state energy storage devices with high energy density.

RESULTS AND DISCUSSION

Synthesis and Characterization of $ZnCo_{1.5}(OH)_{4.5}Cl_{0.5}{\cdot}0.45H_2O$ Nanosheets. The Zn−Co hydroxide sample was prepared by a homogeneous precipitation of dilute $CoCl_2{\cdot}6H_2O$ $ZnCl_2$ solutions in a refluxing process with a high yield of ∼91%. After a refluxing reaction under an optimized condition, the precipitate with a light-blue color can be clearly observed, as shown in Figure 1a,b. Note that the agitated aqueous suspension shows clear anisotropic streams that imply the formation of ordered structures at the macroscopic scale, suggesting anisotropic morphology and high aspect ratios of the as-prepared sample. Elemental analysis and thermogravimetric measurement showed the chemical composition of the obtained sample to be $[ZnCo_{1.5}(OH)_{4.5}Cl_{0.5}{\cdot}0.45H_2O]$ (Anal. calcd (%): Zn, 25.53; Co, 34.51; OH, 29.88; Cl, 6.92; H_2O, 3.16; found (%): Zn, 25.6; Co, 34.6; OH, 29.8; Cl, 6.8; H_2O, 3.2). The number of intercalated water molecules was calculated to be 0.45 according to thermogravimetric analysis (Figure S1). This composition gives a Zn/Co molar ratio of ∼1.50 and an empirical formula weight of 256.2. Accordingly, the formation of $ZnCo_{1.5}(OH)_{4.5}Cl_{0.5}{\cdot}0.45H_2O$ was mainly through the following reactions.

(i) HMT is hydrolyzed at a refluxing temperature:[35]

$$(CH_2)_6N_4 + 6H_2O \rightarrow 6HCHO + 4NH_3$$

(ii) The generated NH_3 reacts with H_2O to create OH^-:

$$NH_3 + H_2O \rightarrow NH_4^+ + OH^-$$

(iii) The Zn^{2+} and Co^{2+} ions react with OH^- and Cl^- ions:

$$Zn^{2+} + 1.5Co^{2+} + 4.5OH^- + 0.5Cl^- + 0.45H_2O \rightarrow ZnCo_{1.5}(OH)_{4.5}Cl_{0.5}{\cdot}0.45H_2O$$

Figure 1c shows X-ray powder diffraction (XRPD, λ = 0.6884 Å) pattern of the as-synthesized sample measured at the powder diffraction beamline, Australian Synchrotron. However, search of the diffraction peaks cannot match with any known crystal structure in the ICDD PDF4 database (2017), suggesting a new phase of the present compound. A systematic absence of $h = 2n + 1$ for $00h$ and index of peaks suggests $P31c$ to be a possible space group. Its layered structure is solved by charge flipping combined with direct space method in TOPAS software 5.0 (Bruker). Rietveld refinement of the synchrotron XRPD pattern with the final refinement results of R_{wp} = 7.8%, R_p = 6.4%, and GoF = 1.43 shows a good fit of the structure model with experimental data. As shown in Figure 1c and Figure S2, all the diffraction peaks could be indexed as a hexagonal structure with a = 6.2878(5) Å, c = 15.2954(2) Å, α = 90°, and γ = 120°. No peaks of impurities were observed, indicating the high purity of the sample. The refined crystallographic information and atomic coordinates are listed in Table 1. Note that the H atoms cannot be located from XRPD data due to their weak scattering from the X-ray.

Table 1. Refined Structure Parameters for $ZnCo_{1.5}(OH)_{4.5}Cl_{0.5}{\cdot}0.45H_2O$ Listing Fractional Coordinates (x, y, z) and Occupancies (Occ.)[a]

atom	x	y	z	Occ.
Zn1	0	0	0.297	1
Zn2	0	0	0.558	1
Co1	0.507	0.004	0.689	1
O1	0.333	0.667	0.620	1
O2	0.173	0.334	0.763	1
O3	0.471	0.504	0.312	0.661
O4	0.836	0.667	0.608	1
Cl1	0.667	0.333	0.440	1

[a]Space group: $P31c$ (no. 159). Unit cell parameters: a = 6.2878(5), b = 6. 2878(5), c = 15.395(2) Å.

The refinement results revealed some important structural features of the layered $ZnCo_{1.5}(OH)_{4.5}Cl_{0.5}{\cdot}0.45H_2O$. The crystal structure is built on $[ZnCo_{1.5}(OH)_{4.5}]^{0.5+}$ cationic layers with chloride ions residing between layers to compensate for the positive charge, as shown in Figure 1d. Water molecules are located at unfixed positions between layers. In detail, there is only one crystallographic site for the Co cations: the one occupies (0.507, 0.004, 0.689) site with six-coordination to six hydroxy groups forming a strongly distorted $[Co(OH)_6]$ octahedron. In each $[Co(OH)_6]$ octahedron, the metal Co atom displaced from the center on the c-axis gives rise to six

DOI: 10.1021/acsnano.8b00653
ACS Nano 2018, 12, 2968−2979

different Co···O bonds within a distance range of 1.888 (12), 2.10(4), 2.120(8), 2.15(5), 2.20(4), and 2.22 (6) Å. Meanwhile, the Zn atoms reside on crystallographic sites with three-coordination to three hydroxyl groups to form a $[Zn(OH)_3]$ trigonal pyramidal. The Zn···O distance in the three-coordination environments is 1.89(5) Å. In the *ab* plane, each $[Co(OH)_6]$ octahedron shares an edge with two adjacent $[Co(OH)_6]$ octahedra, forming a $3[Co(OH)_6]$ octahedra assembly. Each $[Zn(OH)_3]$ trigonal pyramidal stays in the interstitial site between the $[Co(OH)_6]$ octahedra assemblies (Figure 1e). These linked polyhedron units form a 2D $[ZnCo_{1.5}(OH)_{4.5}]^{0.5+}$ host layer stacking along the *c*-axis by an ABABAB pattern. The Cl^- ions and water molecules reside in the gallery between two adjacent $[ZnCo_{1.5}(OH)_{4.5}]^{0.5+}$ host layers (Figure S3) as a charge balance in the structure. We tried to replace the intercalated Cl^- ions with the other interlayer anions through a typical anion-exchange process.[14] However, the anion-exchange behavior cannot be observed in our sample, which is evident by the unchanged XRPD pattern of anion-exchanged samples (Figure S4). This result is quite different than that in previously reported LDH compounds,[14] implying the Cl^- ions have a strong interaction with the nearer host layer in the present $ZnCo_{1.5}(OH)_{4.5}Cl_{0.5}\cdot 0.45H_2O$ crystal. The electron-density distribution is visualized in Figure 1f, which corresponds well with the atomic structure model. Note that the electron density corresponding to the interlayer Cl^- ions has a slightly distorted spherical distribution, which also suggests that the Cl^- ions are bonded with the hydroxide layers. Such a result has been reported in layered rare-earth hydroxide $Re(OH)_{2.5}Cl_{0.5}\cdot 0.8H_2O$ recently.[36]

Figure 2a shows typical scanning electron microscope (SEM) images of $ZnCo_{1.5}(OH)_{4.5}Cl_{0.5}\cdot 0.45H_2O$ nanosheets. The sample consists of numerous well-defined platelets with uniform hexagonal shape and lateral size in the range of 2−4 μm. Obviously, the sample is of high quality in terms of morphology, size, uniformity, and crystallinity, which could be attributed to a slow and homogeneous nucleation process due to the slow hydrolysis of HMT. Figure 2b shows a transmission electron microscopy (TEM) image of the synthesized $ZnCo_{1.5}(OH)_{4.5}Cl_{0.5}\cdot 0.45H_2O$ nanosheets, indicating distinctly that the sample exhibits a well-defined hexagonal shape with the angles of the adjacent edge being about 120°. The selected area electron diffraction (SAED) pattern (Figure 2c) taken from an individual platelet normal to the hexagon surface shows sharp hexagonally arranged diffraction spots, demonstrating its single-crystal nature. This SAED pattern can be readily indexed as the 2D in-plane reflections with the [001] zone axis direction. The observed diffraction spots of the [001] zone axis indicate that each $ZnCo_{1.5}(OH)_{4.5}Cl_{0.5}\cdot 0.45H_2O$ nanosheet is a single crystal with the top (001) surface. A representative high-resolution TEM (HRTEM) image (Figure 2d) shows clear fringe spacing of 2.8 and 2.9 Å, which can be ascribed to (100) and (010) planes of the sample, respectively. The energy-dispersive X-ray spectroscopy (EDS) mapping images show a homogeneous dispersion of cobalt, zinc, and oxygen elements of the nanosheet (Figure S5). The N_2 adsorption−desorption result indicates a Brunauer−Emmett−Teller surface area of ~17.3 $m^2 g^{-1}$, and the pore size distributions ranges from 1.9 to 4.0 nm (Figure S6). Note that the samples are semitransparent under TEM observation, indicating that the e-beam can penetrate the sample due to their ultrathin thickness. Its thickness is estimated to be ≈30 nm by the atomic force microscopy (AFM) image (Figure 2e). Thus, the aspect ratio of the present

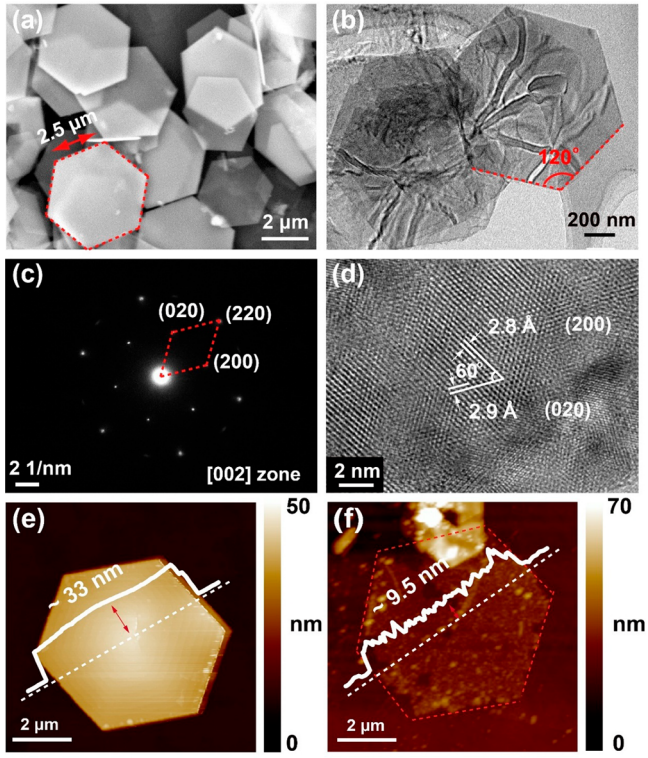

Figure 2. Typical (a) SEM and (b) TEM images of $ZnCo_{1.5}(OH)_{4.5}Cl_{0.5}\cdot 0.45H_2O$ hexagonal nanosheets. (c) SAED patterns taken from the individual one. (d) HRTEM images of the corresponding nanosheet surface. AFM image and height information on (e) $ZnCo_{1.5}(OH)_{4.5}Cl_{0.5}\cdot 0.45H_2O$ bulk and (f) as-exfoliated object.

nanosheet is as high as ~100, which is consistent with the appearance of clear anisotropic streams in the aqueous dispersion, as shown in Figure 1a. We tried to realize the exfoliation of this $ZnCo_{1.5}(OH)_{4.5}Cl_{0.5}\cdot 0.45H_2O$ bulk into a unilamellar structure with single-atom thickness by an ultrasonic treatment in formamide solution reported previously.[37] Unfortunately, the swelling and delamination behavior was not observed due to the strong interaction between the interlayer Cl anions and the cationic host layer. Interestingly, we found that its thickness could be further decreased by a micromechanical exfoliation strategy (Figure S7). The AFM characterization demonstrates that the nanosheets display a smooth surface with much smaller thickness of ~9.5 nm after the micromechanical exfoliation (Figure 2f).

X-ray photoelectron spectroscopy (XPS) (Figure S8) and Fourier transform infrared spectroscopy (FTIR) measurements (Figure S9) were conducted to further understand the structure and composition information on the present sample. In the high-resolution XPS spectrum (Figure 3a), binding energy fitted to 779.8, 781.8, and 796.2 eV in the Co 2p region are attributed to divalent Co^{2+}. In addition, prominent Co $2P_{3/2}$ satellite bands are ascribed to a high-spin Co^{2+}.[22] The absence of peaks at 778.9 eV for Co^{3+} indicates that the $ZnCo_{1.5}(OH)_{4.5}Cl_{0.5}\cdot 0.45H_2O$ is stable without oxidation under ambient conditions.[38] The peaks located at 1020.6 and 1043.5 eV are assigned to Zn $2P_{3/2}$ and Zn $2P_{1/2}$, respectively (Figure 3b).[28,39] In the O 1s region (Figure 3c), binding energies at 529.5 and 530.0 eV are identified as Co−O/Zn−O and OH groups, respectively. The Cl 2p peaks at 198.0 and 199.4 eV are also distinguishable (Figure 3d). In the FTIR

DOI: 10.1021/acsnano.8b00653
ACS Nano 2018, 12, 2968−2979

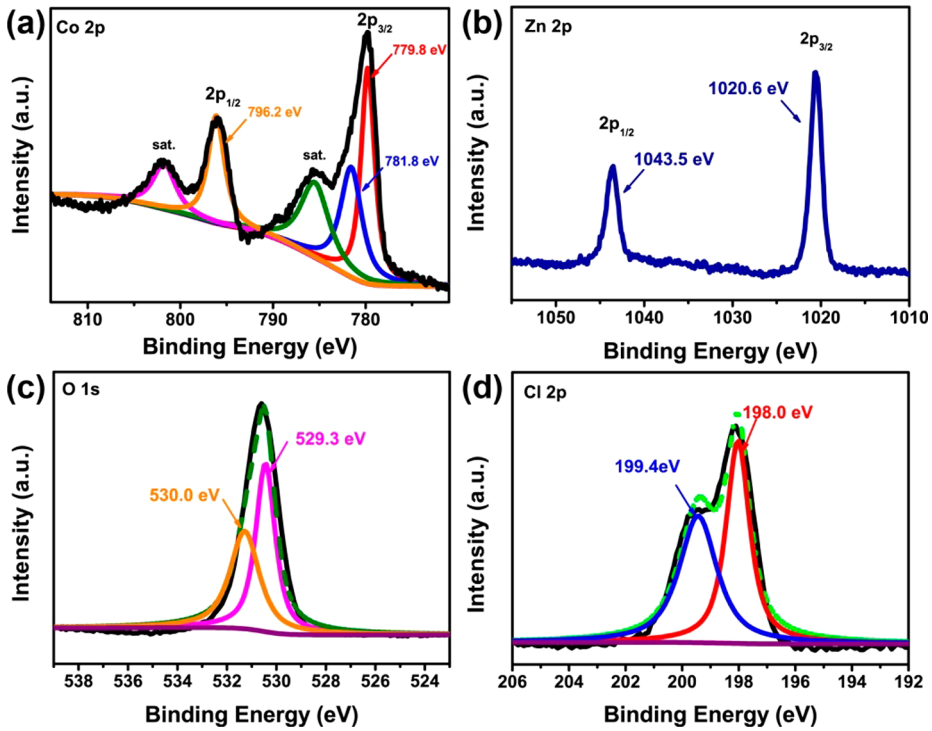

Figure 3. XPS spectra of $ZnCo_{1.5}(OH)_{4.5}Cl_{0.5}{\cdot}0.45H_2O$ powder sample: (a) Co 2p, (b) Zn 2p, (c) O 1s, (d) Cl 2p.

spectra (Figure S9), the absorption bands at 3500 cm^{-1} are ascribed to O−H stretching vibrations of hydrogen-bonded hydroxyl groups and interlayer water molecule, whereas that at 1616 cm^{-1} arises from the bending modes of water molecules. The stretching vibrations at 1045 cm^{-1} are probably assigned to intercalated anions (Cl^-).[29] The absorption peaks below 1000 cm^{-1} are likely associated with Co−O/Zn−O stretching and Co−OH/Zn−OH bending vibrations.[13,40]

To optimize the sample crystallization conditions, various refluxing times and temperatures were chosen. At a shorter refluxing time of 1−3 h, pure $ZnCo_{1.5}(OH)_{4.5}Cl_{0.5}{\cdot}0.45H_2O$ phase can be formed from the XRD pattern in Figure S10. However, only some small-sized objects with irregular shape were found (Figure S11), suggesting the growth process was not accomplished at this condition. Furthermore, at a lower refluxing temperature at 90 °C, the corresponding SEM images (Figure S11d) indicate the presence of some tiny nanoparticles. We also used urea as the alkali source instead of HMT under a refluxing reaction at 120 °C for 5 h. However, the product shows very low crystallinity with rather weak X-ray diffraction peaks, which may be due to the lower reducing power of urea compared with that of HMT (Figure S12).[40] The effect of the concentration of HMT was also investigated. When the concentration of HMT doubled to 90 mM, the $ZnCo_{1.5}(OH)_{4.5}Cl_{0.5}{\cdot}0.45H_2O$ phase can also be formed (Figure S13a) with morphology of significant agglomeration of nanosheets (Figure S13b). Accordingly, the reaction conditions for the growth of high-quality $ZnCo_{1.5}(OH)_{4.5}Cl_{0.5}{\cdot}0.45H_2O$ hexagonal nanosheets was optimized as a homogeneous precipitation at 120 °C for 5 h using 45 mM HMT as the alkali source.

Electrochemical Properties of $ZnCo_{1.5}(OH)_{4.5}Cl_{0.5}{\cdot}0.45H_2O$ Electrodes. To examine the electrochemical properties, the arrays of $ZnCo_{1.5}(OH)_{4.5}Cl_{0.5}{\cdot}0.45H_2O$ nanosheets were *in situ* grown on a 3D macroporous Ni foam substrate by hanging a clean Ni foam substrate into the reaction solution during the aforementioned refluxing process. The color of nickel foam turned light blue accompanied by $ZnCo_{1.5}(OH)_{4.5}Cl_{0.5}{\cdot}0.45H_2O$ nanosheets growing. In the XRD pattern (Figure 4a) of the $ZnCo_{1.5}(OH)_{4.5}Cl_{0.5}{\cdot}0.45H_2O$ nanosheets@Ni foam sample, except for two sharp peaks that originated from Ni foam, the other weak peaks at 2θ values of 11.6, 28.4, and 35.0° can be matched with (002), (110), and (020) reflections of $ZnCo_{1.5}(OH)_{4.5}Cl_{0.5}{\cdot}0.45H_2O$ nanosheets, respectively. Further confirmed by the SEM observation (Figure 4b), the Ni foam substrate is densely covered with arrays of numerous $ZnCo_{1.5}(OH)_{4.5}Cl_{0.5}{\cdot}0.45H_2O$ nanosheets perpendicularly intersecting and aligned. The perpendicular arrays directly growing on the surface of Ni foam generally lead to better charge transport and ion diffusion without any blocks of polymer binders compared with that of the conventional thin film electrode preparation.[10] Subsequently, cyclic voltammograms (CVs), galvanostatic Nyquist, and galvanostatic charge−discharge tests were carried out to investigate the pseudocapacitive behavior of $ZnCo_{1.5}(OH)_{4.5}Cl_{0.5}{\cdot}0.45H_2O$ nanosheets@Ni foam in 1 M KOH aqueous solution. Figure 4c shows the typical CV curves of the as-obtained film at different scan rates. The redox peaks within 0.2−0.5 V correspond to two reversible reactions:[28,41]

$$2ZnCo_{1.5}(OH)_{4.5}Cl_{0.5}{\cdot}0.45H_2O \leftrightarrow 3CoOOH + 3.9H_2O + 2Zn^{2+} + Cl^- + 3e^-$$

$$CoOOH + OH^- \leftrightarrow CoO_2 + H_2O + e^-$$

According to these equations, the theoretical pseudocapacitance of $ZnCo_{1.5}(OH)_{4.5}Cl_{0.5}{\cdot}0.45H_2O$ compound is calculated to be 2259.6 F g^{-1}. As the scan rate increases, the positions of oxidation and reduction peaks shift accordingly to more anodic and cathodic directions, respectively, indicating the kinetic irreversibility as a result of polarization and ohmic resistance

DOI: 10.1021/acsnano.8b00653
ACS Nano 2018, 12, 2968−2979

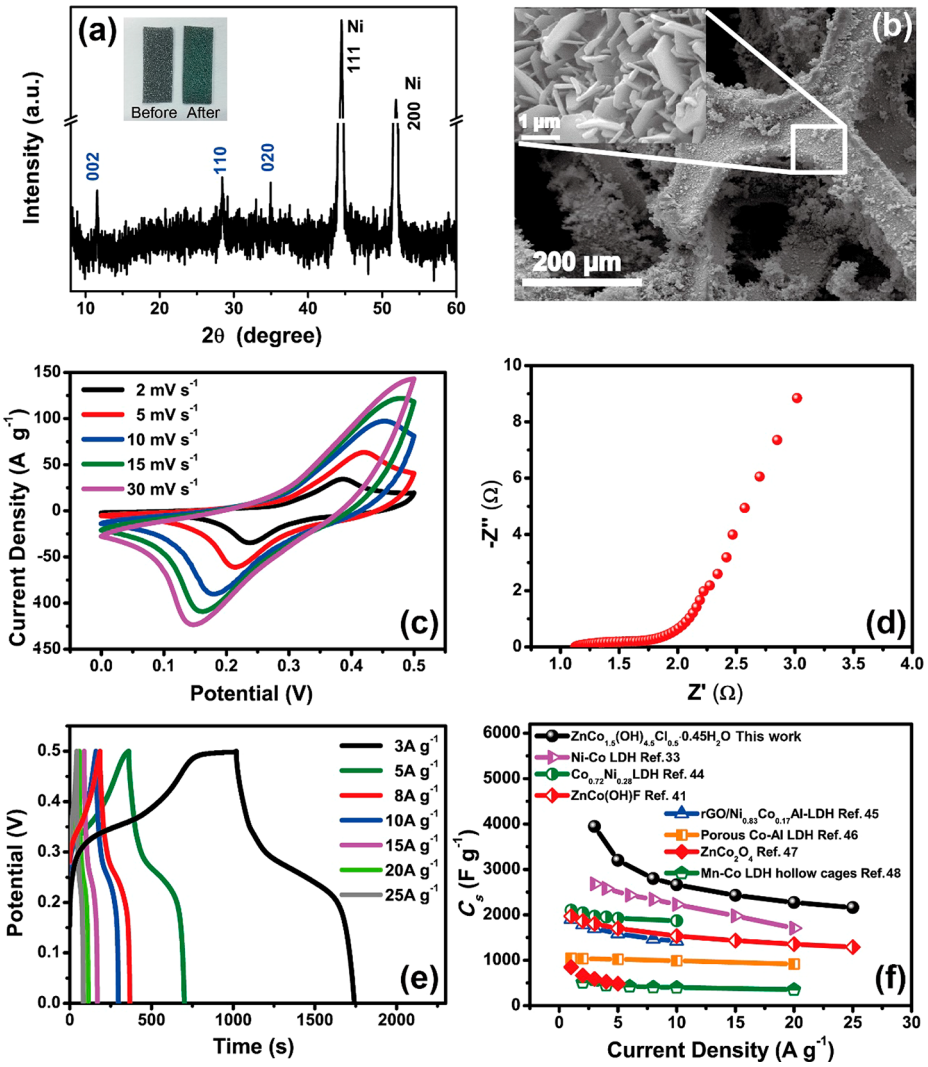

Figure 4. (a) XRD pattern with optical photograph (inset) of $ZnCo_{1.5}(OH)_{4.5}Cl_{0.5}\cdot 0.45H_2O$ nanosheet arrays growing on Ni foam. (b) Typical SEM image of the $ZnCo_{1.5}(OH)_{4.5}Cl_{0.5}\cdot 0.45H_2O$ nanosheet arrays aligned on Ni foam. (c) CV curves of the $ZnCo_{1.5}(OH)_{4.5}Cl_{0.5}\cdot 0.45H_2O$ nanosheets electrode at different scan rates. (d) Nyquist plot of the $ZnCo_{1.5}(OH)_{4.5}Cl_{0.5}\cdot 0.45H_2O$ nanosheet electrode. (e) Galvanostatic charge–discharge curves and (f) comparison of C_s of the $ZnCo_{1.5}(OH)_{4.5}Cl_{0.5}\cdot 0.45H_2O$ and previously reported transition metal oxide/hydroxide electrodes at varied current densities.

during the Faradaic process.[42] A Nyquist plot in Figure 4d demonstrates that the series resistance (R_s, the real axis intercept) of $ZnCo_{1.5}(OH)_{4.5}Cl_{0.5}\cdot 0.45H_2O$ electrode is only 1.4 Ω.[43] This value suggests a low resistance by virtue of the combination of the intrinsic resistance of the active materials, the intrinsic resistance of the substrate, and the contact resistance of the active materials/current collector interface, which may be attributed to the strong affinity of the active materials and the nickel foam through a one-step growth method.[45] Figure 4e shows the galvanostatic charge–discharge curves of the electrode at different current densities (from 3 to 25 A g^{-1}) over the voltage window of 0–0.5 V, and all curves are nonlinear lines, suggesting strong pseudocapactive behavior of the active materials. The specific capacitances of the electrodes are as high as 3946.5 F g^{-1} at a scan rate of 3 A g^{-1} and 2160.4 F g^{-1} at a high scan rate of 25 A g^{-1}, which is more than 20 times higher than the thin film staked by Zn–Co LDHs nanosheets reported previously.[32] This value also exceeds that of previously reported transition metal oxides/hydroxides (Figure 4f), including Ni–Co LDH (2682 F g^{-1} at 3 A g^{-1} and 1706 F g^{-1} at 20 A g^{-1}),[33] $Co_{0.72}Ni_{0.28}$ LDH (2104 F g^{-1} at 1 A g^{-1} and 1870 F g^{-1} at 10 A g^{-1}),[44] Zn–Co(OH)F nanoneedles (1808 F g^{-1} at 3 A g^{-1} and 1354 F g^{-1} at 20 A g^{-1}),[41] rGO/$Ni_{0.83}Co_{0.17}$Al-LDH (1701 F g^{-1} at 3 A g^{-1} and 1442 F g^{-1} at 10 A g^{-1}),[45] porous Co–Al LDH (1034 F g^{-1} at 2 A g^{-1} and 916 F g^{-1} at 20 A g^{-1}),[46] $ZnCo_2O_4$ (851 F g^{-1} at 1 A g^{-1} and 485 F g^{-1} at 5 A g^{-1}),[47] and Mn–Co LDH hollow cages (511 F g^{-1} at 2 A g^{-1} and 356F g^{-1} at 20 A g^{-1}).[48] The energy densities of the as-obtained $ZnCo_{1.5}(OH)_{4.5}Cl_{0.5}\cdot 0.45H_2O$ nanosheet electrodes are calculated to be 144.7 and 50.5 Wh kg^{-1} at average power densities of 721.4 and 4582.9 W kg^{-1}, respectively.

Note that the specific capacitance calculated from the GCD curve is higher than the theoretical pseudocapacitance, which has also been usually observed in other material series.[41,49,50] Jin *et al.* reported that single-layer β-$Co(OH)_2$ nanosheets exhibit specific capacitance up to 3355 F g^{-1}, which is much higher than the theoretical value of 2590 F g^{-1}.[50] Herein, we propose the high performance of the $ZnCo_{1.5}(OH)_{4.5}Cl_{0.5}\cdot 0.45H_2O$ nanosheet arrays would be attributed to the following

DOI: 10.1021/acsnano.8b00653
ACS Nano 2018, 12, 2968–2979

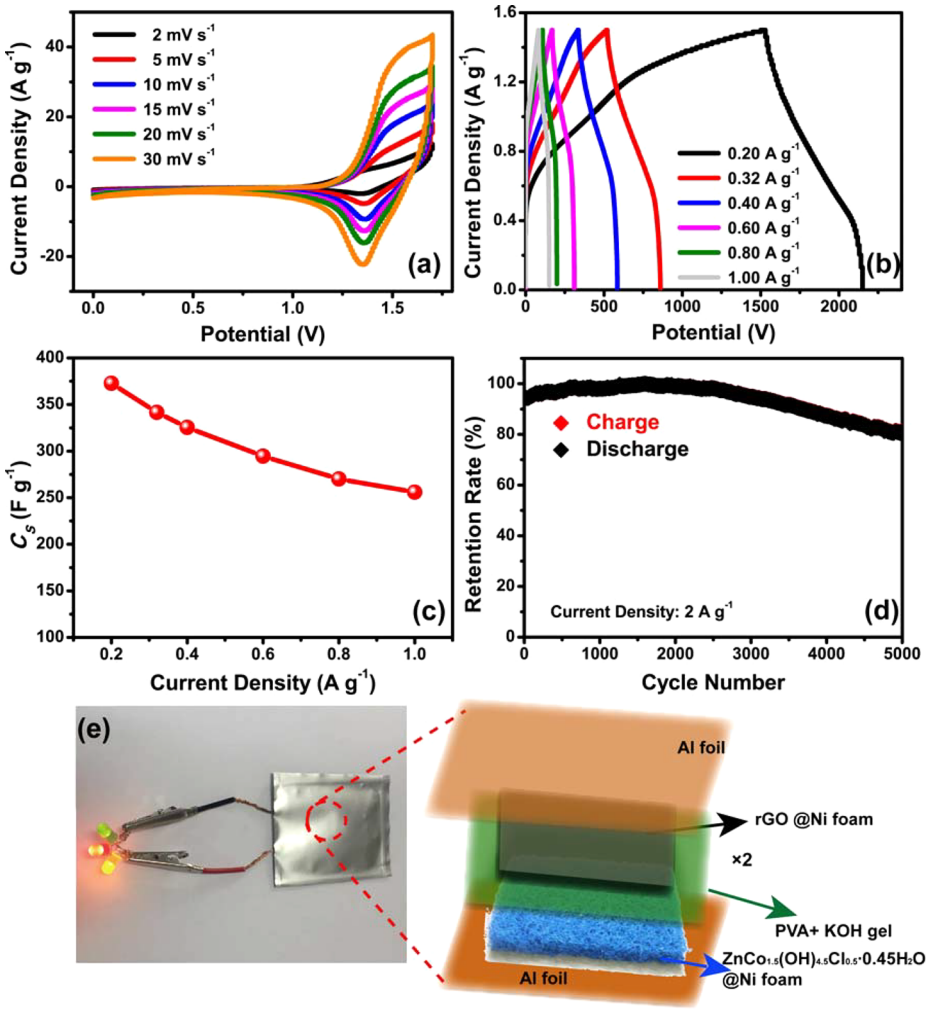

Figure 5. (a) CV curves of the $ZnCo_{1.5}(OH)_{4.5}Cl_{0.5}\cdot 0.45H_2O$//PVA- KOH//rGO asymmetric supercapacitor at different scan rates. (b) Galvanostatic charge−discharge curves and (c) C_s of the asymmetric supercapacitor at different current densities. (d) Cycling performance of the asymmetric supercapacitor. (e) Photographs (left) and schematic illustration (right) of the light-emitting diode indicators lighted by two supercapacitors connected in series.

aspects: (1) Unique layered crystal structure. The interlayer distance of the layered $ZnCo_{1.5}(OH)_{4.5}Cl_{0.5}\cdot 0.45H_2O$ crystal is ∼1.53 nm. Such a distance can be regarded as "ion-buffer reservoirs" of electrolyte ions during the electrochemical process.[50] Furthermore, the highly exposed (001) surface of $ZnCo_{1.5}(OH)_{4.5}Cl_{0.5}\cdot 0.45H_2O$ nanosheets provides more active sites for charge storage, also leading to a high specific capacitance.[51] (2) Synergistic effect between Zn and Co. The Zn^{2+} ions in $ZnCo_{1.5}(OH)_{4.5}Cl_{0.5}\cdot 0.45H_2O$ compound might play some roles by assisting the electron transportation in accessing the highly oxidized Co ion in the material, thereby endowing a more efficient pseudocapacitive process.[30,41] (3) 2D morphology with nanoscale thinness (∼30 nm). This ultrathin thickness should greatly shorten the ion diffusion paths, which are favorable for fast redox reactions. (4) *In situ* growth and binder-free design on Ni foam. The success of *in situ* growth results in strong affinity and small charge resistance between the substrate and the active materials. This characteristic facilitates the kinetics at the electrode interfaces, exhibiting superior electron mobility during the electrochemical process. (5) The contribution of electrochemical double-layer capacitance. It is known that double-layer capacitance performance of layered materials is quite inseparable from their morphology.[52] Herein, our $ZnCo_{1.5}(OH)_{4.5}Cl_{0.5}\cdot 0.45H_2O$ nanosheets show high specific surface area, which would produce electrochemical double-layer capacitance.[53]

All-solid-state asymmetric supercapacitors with $ZnCo_{1.5}(OH)_{4.5}Cl_{0.5}\cdot 0.45H_2O$ nanosheets@Ni foam as the positive electrode, rGO as the negative electrode, and poly(vinyl alcohol) (PVA)−KOH gel as electrolyte were fabricated subsequently. Based on the specific capacitance (C_s), the working potential of the $ZnCo_{1.5}(OH)_{4.5}Cl_{0.5}\cdot 0.45H_2O$ electrode and rGO electrode (Figure S14), as well as the principle of charge balance between the two electrodes, the mass ratio of $ZnCo_{1.5}(OH)_{4.5}Cl_{0.5}\cdot 0.45H_2O$ to rGO was optimized at about 1:13 in the asymmetric supercapacitor cell.[33] As shown in the CV curve acquired at a variety of scan rates (Figure 5a), the rGO electrode shows rather lower capacitance compared with the positive electrode. Figure 5b presents the galvanostatic charge−discharge curves of the supercapacitor at charge−discharge current densities from 0.20 to 1.00 A g^{-1}. The C_s of the $ZnCo_{1.5}(OH)_{4.5}Cl_{0.5}\cdot 0.45H_2O$//(PVA)−KOH gel//rGO device was calculated to be 344.9, 341.6, 325.38, 294.6, 270.0, and 255.8 F g^{-1} at current densities of 0.20, 0.32, 0.40, 0.60, 0.80, and 1.00 A g^{-1} based on active materials in the positive and negative electrodes, as shown in

DOI: 10.1021/acsnano.8b00653
ACS Nano 2018, 12, 2968−2979

Figure 5c, which is superior to that of recently reported all-solid-state supercapacitors, listed in Table S1.The cyclic galvanostatic charge−discharge test was further carried out to evaluate the durability and stability of the as-fabricated all-solid-state asymmetric supercapacitor. As can be seen in Figure 5d, it can still retain about 81% of its original capacitance even after 5000 cycles at a charge−discharge current density of 2.00 A g^{-1}. The Ragone diagram plotting the energy and power densities of the as-fabricated supercapacitor is described in Figure 6, which

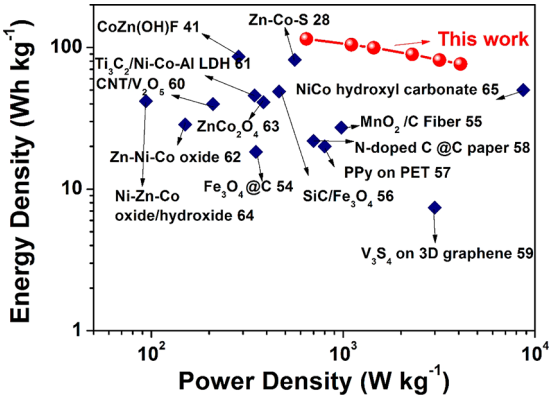

Figure 6. Comparison of the energy densities *vs* power density curves of $ZnCo_{1.5}(OH)_{4.5}Cl_{0.5}{\cdot}0.45H_2O$//PVA-KOH//rGO and recently reported all-solid-state supercapacitors.[54−65]

is calculated based on the galvanostatic discharge plots. Based on the total mass of the materials, the maximum energy density of the asymmetric supercapacitor is 114.8 Wh kg^{-1} at 643.8 W kg^{-1} and still retains 76.4 Wh kg^{-1} at 4085.1 W kg^{-1}, which surpasses that of most recently reported all-solid-state supercapacitors constructed from carbonaceous materials, transition metal oxides/hydroxides, and MXenes (Table S2). Figure 5e shows that three light-emitting diode indicators with different colors were lighted by two supercapacitors connected in series.

Taking advantage of the ultrathin nature and well-defined 2D morphology, we consider that $ZnCo_{1.5}(OH)_{4.5}Cl_{0.5}{\cdot}0.45H_2O$ nanosheets could be used as the anode materials in flexible energy storage devices.[2] To check out the flexibility and mechanical stability of the solid-state devices, a flexible symmetric supercapacitor was fabricated based on PET substrate. It was folded or bent at various angles from 0 to 120°, and the corresponding electrochemical responses were recorded as shown in Figure 7c−f. Compared with the CV curve at a scan rate of 200 mV s^{-1} without folding or bending (Figure 7a), the CV curve remains nearly unchanged when bent to 60°. At higher bending curvature of 90 and 120°, the CV curves are still identical to the unbent one. These results manifest that the $ZnCo_{1.5}(OH)_{4.5}Cl_{0.5}{\cdot}0.45H_2O$@PET-based supercapacitors have potential to develop high-performance flexible and gadget devices.

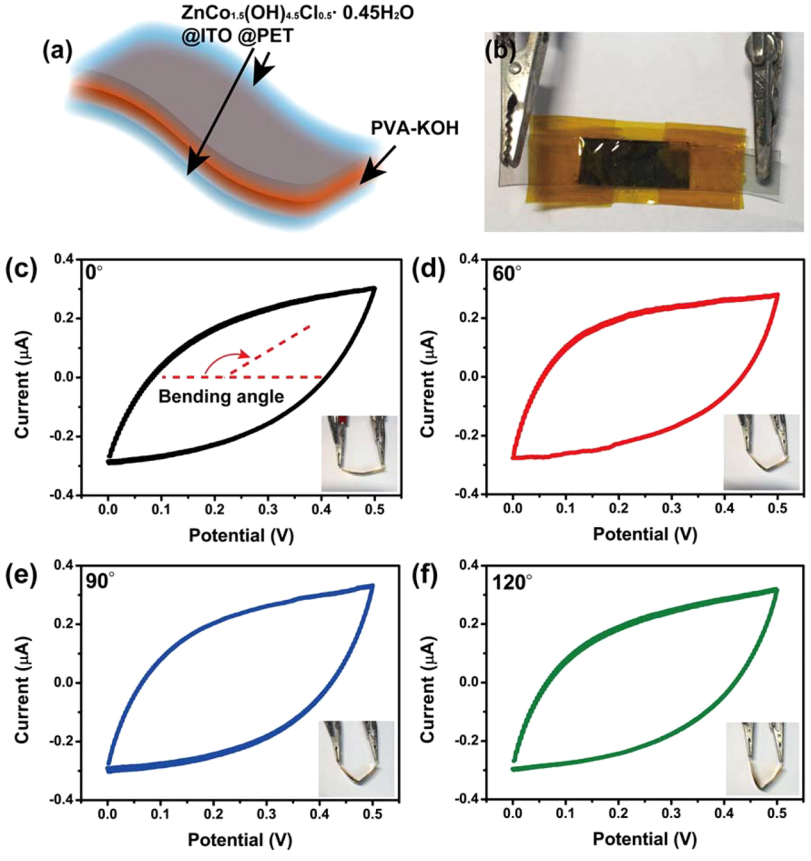

Figure 7. (a) Schematic diagrams and (b) photograph of the $ZnCo_{1.5}(OH)_{4.5}Cl_{0.5}{\cdot}0.45H_2O$@PET-based symmetric supercapacitor. CV curves at different bending angles: (c) 0°, (d) 60°, (e) 90°, and (f) 120°, showing the flexibility and mechanical stability of the symmetric flexible supercapacitor.

DOI: 10.1021/acsnano.8b00653
ACS Nano 2018, 12, 2968−2979

CONCLUSION

In summary, the layered $ZnCo_{1.5}(OH)_{4.5}Cl_{0.5}\cdot 0.45H_2O$ nanosheet is a promising electrode material for high-performance, flexible, all-solid-state supercapacitors. It could be prepared in high purity and large scale through a facile homogeneous precipitation strategy and spontaneously crystallized into typical 2D hexagonal morphology, with the crystal structure revealed by synchrotron X-ray powder diffraction data analysis. The $ZnCo_{1.5}(OH)_{4.5}Cl_{0.5}\cdot 0.45H_2O$ nanosheet electrode obtained by *in situ* growth synthesis on Ni foam exhibits a very high specific capacitance of 3946.5 F g^{-1} at 3 A g^{-1}. The $ZnCo_{1.5}(OH)_{4.5}Cl_{0.5}\cdot 0.45H_2O$ nanosheets@Ni foam//PVA, KOH//rGO-based all-solid-state asymmetric supercapacitor exhibited a high energy density of 114.8 Wh kg^{-1} at a power density of 643.8 W kg^{-1}, which exceeded most reported asymmetric supercapacitors constructed from carbonaceous materials, transition metal oxides/hydroxides, and MXenes. Furthermore, a device based on $ZnCo_{1.5}(OH)_{4.5}Cl_{0.5}\cdot 0.45H_2O$ nanosheets@PET//PVA, KOH//$ZnCo_{1.5}(OH)_{4.5}Cl_{0.5}\cdot 0.45H_2O$ nanosheets@PET showed excellent flexibility and mechanical stability. The present study provides layered Zn–Co bimetallic hydroxide nanosheets as promising electroactive materials for flexible, solid-state energy storage devices, presenting the best reported performance to date. In the next work, we will continue to optimize the pseudocapacitance behavior of this layered compound by controllable Zn/Co atomic ratios, and the development of their hydrogen evolution reaction and oxygen evolution reaction properties would be interesting, as well.

EXPERIMENTAL SECTION

Synthesis of $ZnCo_{1.5}(OH)_{4.5}Cl_{0.5}\cdot 0.45H_2O$. Before the synthesis, 1 dm^3 of deionized water was treated with a nitrogen flow for 30 min to remove the dissolved CO_3^{2-} and then transferred into a three-neck flask equipped with a reflux condenser. In a typical procedure for synthesis, $CoCl_2\cdot 6H_2O$, $ZnCl_2$, and hexamethylenetetramine (HMT) were dissolved in 1 dm^3 of deionized water to give the final concentrations of 3, 2, and 45 mM, respectively. Then, the mixed solution was heated to a refluxing temperature of 120 °C under continuous magnetic stirring for 5 h. A nitrogen flow was applied to prevent the water from boiling during the refluxing. The resulting light blue product was filtered, washed with deionized water and anhydrous alcohol over five times, and eventually dried in an oven at 60 °C.

Exfoliation. For the ion-exchange process, the as-synthesized $ZnCo_{1.5}(OH)_{4.5}Cl_{0.5}\cdot 0.45H_2O$ powder was added in a salt–acid mixed solution according to the method reported previously.[21] In a typical procedure, 0.5 M sodium dodecyl sulfate ($C_{12}H_{25}OSO_3Na$) (or 0.5 M $NaNO_3$) and 2 mM HCl were dispersed into 100 mL of a water/ethanol (1:1, v/v) binary solution. The as-obtained suspension was shaken for 48 h at 180 rpm. For mechanical exfoliation, the $ZnCo_{1.5}(OH)_{4.5}Cl_{0.5}\cdot 0.45H_2O$ powder was exfoliated into ultrathin nanosheets using scotch tape. After a repeated peeling-off process, the sample becomes thinner and thinner as one repeats this for numerous times. The as-exfoliated nanosheets left on the tape were transferred to the silicon substrate for further characterization.

***In Situ* Growth of $ZnCo_{1.5}(OH)_{4.5}Cl_{0.5}\cdot 0.45H_2O$ Nanosheet Array on Ni Foam.** Ni foam (10 mm × 50 mm × 0.1 mm, 110 ppi (pores per inch), 320g m^{-2}) was pretreated successively with acetone, 1 M HCl solution, deionized water, and anhydrous alcohol, each for 15 min ultrasound treatment, to create a clean surface. The cleaned nickel foam was then partially immersed in the solution of the three-neck flask system at a refluxing temperature of 120 °C under continuous magnetic stirring for 5 h. The Ni foam substrate, covered with $ZnCo_{1.5}(OH)_{4.5}Cl_{0.5}\cdot 0.45H_2O$ nanosheets (about 1.1 mg cm^{-2}), was washed with Milli-Q water and ethanol in an ultrasonic bath cleaner and then dried at 80 °C for 12 h. The loading mass of the active materials on Ni foam was determined by subtracting the weight before and after the *in situ* growth, and this measurement was carried out three times to eliminate experimental errors.

Fabrication of the $ZnCo_{1.5}(OH)_{4.5}Cl_{0.5}\cdot 0.45H_2O$//PVA-KOH//rGO All-Solid-State Asymmetric Supercapacitor. The $ZnCo_{1.5}(OH)_{4.5}Cl_{0.5}\cdot 0.45H_2O$ nanosheet electrode assumed to be the positive of the asymmetric supercapacitor was prepared by the aforementioned *in situ* growth method. The negative electrode was made of rGO powder (purchased from Nanjing XF Nanomaterials and Technologies Co. Ltd.; diameter = 0.5–2 μm; thickness ~ 0.8 nm; monolayer ratio ~ 80%; purity ~ 99%). A mixture of rGO powder, 20 wt % acetylene black (as an electrical conductor), 10 wt % polytetrafluorene–ethylene (as a binder), and a small amount of anhydrous ethanol was prepared by milling to produce a homogeneous paste. The paste was then pressed onto the Ni foam current collector to produce the rGO electrode. The above two electrodes were then pressed and combined with each other with PVA gel of KOH (3 M) as the solid electrolyte to assemble the full cell. The cell was encapsulated by flexible Kapton film with two pieces of copper wires connected to the edges of the two electrodes.

Fabrication of the Flexible Supercapacitor. The PET substrates were first deposited onto a layer of ITO film (~5–10 nm thick) and then coated with a layer of slurry containing 75% active materials and 25% acetylene black (ATB) *via* a process similar to that of the rGO electrode and then were dried at 60 °C. Next, two pieces of such electrodes were immersed in the PVA/KOH gel solution for 5–10 min to absorb a layer of electrolyte and then placed in an oven at 40 °C to vaporize the excess water. The symmetric flexible supercapacitor was obtained by pressing two pieces of such electrodes immersed with electrolyte together.

Sample Characterization. Sample morphologies were characterized on a FEI Navo Nano SEM 450 field-emission scanning electron microscopy and a Bruker Dimension Icon atomic force microscopy. Transmission electron microscopy, high-resolution microscopy, and selected area electron diffraction were performed using a Philips CM 200 FEG field-emission microscope at an acceleration voltage of 300 kV. XPS (Kratos Axis Ultra Dld) was employed to investigate the elemental composition and chemical state of the sample. The crystalline structure was studied on a Bruker D8-A25 diffractometer with Cu Kα radiation (λ = 1.5406 Å). For phase identification and structure determination, the synthesized sample was loaded into 0.7 mm quartz capillaries, and synchrotron XRPD data were collected using a Mythen-II detector at powder diffraction beamline, Australian Synchrotron (ANSTO). Two separate collections were undertaken at a wavelength of 0.6884 Å, determined using NIST SRM 660b LaB_6. The surface characteristics of the sample were studied using gas physisorption at 77 K on an automated apparatus (Micromeritics, ASAP 2010). FTIR spectra were measured to study the bonding condition using the KBr pellet technique in the range of 400–4000 cm^{-1}. The Co and Zn contents of the samples were determined by inductively coupled plasma atomic emission spectroscopy (Seiko SPS1700HVR) after dissolving a weighed amount of sample with an aqueous HCl solution. The content of OH was determined according to the back-titration method. Typically, approximately 0.2 g of sample was dissolved in an excess of standard acid solution (0.1 M HCl), and the excess acid was back-titrated with a standard base (0.05 M NaOH) using a pH meter. The Cl^- content was gravimetrically estimated as AgCl after 0.2 g of sample was dissolved in diluted HNO_3 solution. The unaccounted weight belongs to the water content to arrive at an approximate formula, which was verified by thermogravimetric analysis using a SDT Q600 instrument in the temperature range of 25–800 °C at a heating rate of 5 °C min^{-1} under an air flow.

Electrochemical Measurements. The electromechanical properties of the $ZnCo_{1.5}(OH)_{4.5}Cl_{0.5}\cdot 0.45H_2O$ nanosheets were carried out under a three-electrode cell configuration at 25 °C in 1 M KOH. The nickel foam supporting $ZnCo_{1.5}(OH)_{4.5}Cl_{0.5}\cdot 0.45\ H_2O$ nanosheet arrays acted as the working electrodes and were soaked in a 1 M KOH solution and degassed in a vacuum for 5 h before the electrochemical test. Platium foil and a Ag/AgCl electrode were used as the counter and reference electrodes, respectively. The electrochemical impedance

DOI: 10.1021/acsnano.8b00653
ACS Nano 2018, 12, 2968–2979

spectroscopy measurements for the electrode were in the frequency range from 0.01 Hz to 100 kHz at open-circuit voltage with an AC perturbation of 5 mV. The electrochemical properties of asymmetric $ZnCo_{1.5}(OH)_{4.5}Cl_{0.5}{\cdot}0.45H_2O$ @Ni//PVA-KOH//rGO all-solid-state supercapacitor and the symmetric $ZnCo_{1.5}(OH)_{4.5}Cl_{0.5}{\cdot}0.45H_2O$@PET//PVA//$ZnCo_{1.5}(OH)_{4.5}Cl_{0.5}{\cdot}0.45H_2O$ @PET flexible supercapacitor were examined under a two-electrode cell configuration. The cyclic voltammetry, galvanostatic charge−discharge, and electrochemical impedance spectroscopy measurements were conducted on a Gamry 90I electrochemical workstation (Gamry Instrument Company, USA). The specific capacitance of the $ZnCo_{1.5}(OH)_{4.5}Cl_{0.5}{\cdot}0.45H_2O$ nanosheet electrode was calculated from galvanostatic charge−discharge curves as follows: $C_s = I \times \Delta t/(\Delta V \times m)$, where C_s (F g^{-1}) is the specific capacitance, I (A) is the discharge current, Δt (s) is the discharge time, ΔV (V) is the potential change during the discharge process, and m' (g) is the mass of the active material in the electrode. The C_s of the asymmetric all-solid-state supercapacitor was calculated from galvanostatic charge−discharge curves as follows: $C_s = 4 \times I \times \Delta t/(\Delta V \times m')$, wherein m' (g) is the total mass of the active material in the electrodes. The energy and power densities of the $ZnCo_{1.5}(OH)_{4.5}Cl_{0.5}{\cdot}0.45H_2O$ nanosheet electrode and the asymmetric supercapacitor were calculated as follows: $E = 0.5 \times C_s \times V^2$, $P_{ave} = E/\Delta t$, where E (Wh kg^{-1}) is the energy density, V (V) is the cell voltage excluding IR drop, P_{ave} (W kg^{-1}) is the average power density, and Δt (s) is the discharge time. The theoretical pseudocapacitance is calculated as[53]

$$C = \frac{n \times F}{M \times V}$$

where n is the mean number of the electrons transferred in the redox reaction, F is the Faraday constant, M is the molar mass of the metal oxide and V is the operating voltage window.

Calculation method. The plane wave pseudopotential method within density functional theory as implemented in the CASTEP code (Materials Studio 8.0 package) was employed. The exchange−correlation functional was approximated by the generalized gradient approximation of the Perdew−Burke−Ernzerhof type. Ultrasoft pseudopotentials were adopted to describe the core−valence interactions, and the wave functions of the valence electrons were expanded in plane waves with a kinetic energy cutoff of 380 eV. To achieve the accurate density of the electronic states, a 2 × 6 × 6 k-point mesh was used.

ASSOCIATED CONTENT

Supporting Information

The Supporting Information is available free of charge on the ACS Publications website at DOI: 10.1021/acsnano.8b00653.

Additional data and discussion (PDF)

AUTHOR INFORMATION

Corresponding Authors

*E-mail: qinfen.gu@synchrotron.org.au.
*E-mail: dlsun@fudan.edu.cn.
*E-mail: linfenghu@fudan.edu.cn.

ORCID

Linfeng Hu: 0000-0002-0640-508X

Notes

The authors declare no competing financial interest.

ACKNOWLEDGMENTS

This work was financially supported by the National Natural Science Foundation of China (Nos. 51701042, 51372040, 51601040, 51471052, 51571063, and U1201241) and the Shanghai Rising-Star Program (16QA1400700). Part of the experiment was performed at the Powder Diffraction Beamline, Australian Synchrotron.

REFERENCES

(1) Mefford, J. T.; Hardin, W. G.; Dai, S.; Johnston, K. P.; Stevenson, K. J. Anion Charge Storage through Oxygen Intercalation in $LaMnO_3$ Perovskite Pseudocapacitor Electrodes. *Nat. Mater.* **2014**, *13*, 726−732.

(2) Huang, Y.; Zhong, M.; Huang, Y.; Zhu, M.; Pei, Z.; Wang, Z.; Xue, Q.; Xie, X.; Zhi, C. A Self-Healable and Highly Stretchable Supercapacitor Based on a Dual Crosslinked Polyelectrolyte. *Nat. Commun.* **2015**, *6*, 10310.

(3) Huang, Y.; Zhong, M.; Shi, F.; Liu, X.; Tang, Z.; Wang, Y.; Huang, Y.; Hou, H.; Xie, X.; Zhi, C. An Intrinsically Stretchable and Compressible Supercapacitor Containing a Polyacrylamide Hydrogel Electrolyte. *Angew. Chem., Int. Ed.* **2017**, *56*, 9141−9145.

(4) Chen, L. F.; Huang, Z. H.; Liang, H. W.; Yao, W. T.; Yu, Z. Y.; Yu, S. H. Flexible All-Solid-State High-Power Supercapacitor Fabricated with Nitrogen-Doped Carbon Nanofiber Electrode Material Derived from Bacterial Cellulose. *Energy Environ. Sci.* **2013**, *6*, 3331−3338.

(5) Ashok Kumar, N.; Baek, J. B. Electrochemical Supercapacitors from Conducting Polyaniline-graphene Platforms. *Chem. Commun.* **2014**, *50*, 6298−308.

(6) Zhao, H.; Zhou, M.; Wen, L.; Lei, Y. Template-Directed Construction of Nanostructure Arrays for Highly-Efficient Energy Storage and Conversion. *Nano Energy* **2015**, *13*, 790−813.

(7) Jiang, H.; Lee, P. S.; Li, C. 3D Carbon Based Nanostructures for Advanced Supercapacitors. *Energy Environ. Sci.* **2013**, *6*, 41−53.

(8) Zhu, C.; Usiskin, R. E.; Yu, Y.; Maier, J. The Nanoscale Circuitry of Battery Electrodes. *Science* **2017**, *358*, 2808.

(9) Zhao, Y.; Jia, X.; Chen, G.; Shang, L.; Waterhouse, G. I.; Wu, L. Z.; Tung, C. H.; O'Hare, D.; Zhang, T. Ultrafine NiO Nanosheets Stabilized by TiO_2 from Monolayer NiTi-LDH Precursors: An Active Water Oxidation Electrocatalyst. *J. Am. Chem. Soc.* **2016**, *138*, 6517−6524.

(10) Zhang, G. Q.; Lou, X. W. General Solution Growth of Mesoporous $NiCo_2O_4$ Nanosheets on Various Conductive Substrates as High-performance Electrodes for Supercapacitors. *Adv. Mater.* **2013**, *25*, 976−979.

(11) Song, F.; Hu, X. L. Exfoliation of Layered Double Hydroxides for Enhanced Oxygen Evolution Catalysis. *Nat. Commun.* **2014**, *5*, 4477.

(12) Liu, Z. P.; Ma, R. Z.; Osada, M.; Takada, K.; Sasaki, T. Selective and Controlled Synthesis of α-and β-cobalt Hydroxides in Highly Developed Hexagonal Platelets. *J. Am. Chem. Soc.* **2005**, *127*, 13869−13874.

(13) Ma, R.; Takada, K.; Fukuda, K.; Iyi, N.; Bando, Y.; Sasaki, T. Topochemical Synthesis of Monometallic (Co^{2+}−Co^{3+}) Layered Double Hydroxide and Its Exfoliation into Positively Charged $Co(OH)_2$ Nanosheets. *Angew. Chem., Int. Ed.* **2008**, *47*, 86−89.

(14) Ding, K.; Zhang, X.; Li, J.; Yang, P.; Cheng, X. Phase and Morphology Evolution of Ultrathin $Co(OH)_2$ Nanosheets towards Supercapacitor Application. *CrystEngComm* **2017**, *19*, 5780−5786.

(15) Wang, H. L.; Robinson, J. T.; Diankov, G.; Dai, H. Nanocrystal Growth on Graphene with Various Degrees of Oxidation. *J. Am. Chem. Soc.* **2010**, *132*, 3270−3271.

(16) Wang, H. L.; Casalongue, H. S.; Liang, Y. Y.; Dai, H. J. $Mn_3O_4^-$ Graphene Hybrid as a High-Capacity Anode Material for Lithium Ion Batteries. *J. Am. Chem. Soc.* **2010**, *132*, 7472−7477.

(17) Zhao, J. W.; Chen, J.; Xu, S. M.; Shao, M. F.; Zhang, Q.; Wei, F.; Ma, J.; Wei, M.; Evans, D. G.; Duan, X. Hierarchical NiMn Layered Double Hydroxide/Carbon Nanotubes Architecture with Superb Energy Density for Flexible Supercapacitors. *Adv. Funct. Mater.* **2014**, *24*, 2938−2946.

(18) Ma, R.; Liu, X. H.; Liang, J. B.; Bando, Y.; Sasaki, T. Molecular-Scale Heteroassembly of Redoxable Hydroxide Nanosheets and Conductive Graphene into Superlattice Composites for High-Performance Supercapacitors. *Adv. Mater.* **2014**, *26*, 4173−4178.

(19) Liu, X. H.; Ma, R.; Bando, Y.; Sasaki, T. High-Yield Preparation, Versatile Structural Modification, and Properties of Layered Cobalt Hydroxide Nanocones. *Adv. Funct. Mater.* **2014**, *24*, 4292−4302.

DOI: 10.1021/acsnano.8b00653
ACS Nano 2018, 12, 2968−2979

(20) Liu, Z. P.; Ma, R.; Osada, M.; Iyi, N.; Ebina, Y.; Takada, K.; Sasaki, T. Synthesis, Anion Exchange, and Delamination of Co−Al Layered Double Hydroxide: Assembly of the Exfoliated Nanosheet/Polyanion Composite Films and Magneto-Optical Studies. *J. Am. Chem. Soc.* **2006**, *128*, 4872−4880.
(21) Ma, R.; Liu, Z. P.; Takada, K.; Iyi, N.; Bando, Y.; Sasaki, T. Synthesis, Anion Exchange, and Delamination of Co−Al Layered Double Hydroxide: Assembly of the Exfoliated Nanosheet/Polyanion Composite Films and Magneto-Optical Studies. *J. Am. Chem. Soc.* **2007**, *129*, 5257−5263.
(22) Ma, R.; Liang, J.; Takada, K.; Sasaki, T. Topochemical Synthesis of Co−Fe Layered Double Hydroxides at Varied Fe/Co Ratios: Unique Intercalation of Triiodide and Its Profound Effect. *J. Am. Chem. Soc.* **2011**, *133*, 613−620.
(23) Ma, R.; Liang, J.; Liu, X. H.; Sasaki, T. General Insights into Structural Evolution of Layered Double Hydroxide: Underlying Aspects in Topochemical Transformation from Brucite to Layered Double Hydroxide. *J. Am. Chem. Soc.* **2012**, *134*, 19915−19921.
(24) Sun, P.; Ma, R.; Bai, X.; Wang, K.; Zhu, H.; Sasaki, T. Single-Layer Nanosheets with Exceptionally High and Anisotropic Hydroxyl Ion Conductivity. *Sci. Adv.* **2017**, *3*, e1602629.
(25) Jia, Y.; Zhang, L. Z.; Gao, G. P.; Chen, H.; Wang, B.; Zhou, J. Z.; Soo, M. T.; Hong, M.; Yan, X. C.; Qian, G. R.; Zou, J.; Du, A. J.; Yao, X. D. A Heterostructure Coupling of Exfoliated Ni-Fe Hydroxide Nanosheet and Defective Graphene as a Bifunctional Electrocatalyst for Overall Water Splitting. *Adv. Mater.* **2017**, *29*, 1700017.
(26) Chen, Y.; Pang, W. K.; Bai, H.; Zhou, T.; Liu, Y.; Li, S.; Guo, Z. Enhanced Structural Stability of Nickel−Cobalt Hydroxide *via* Intrinsic Pillar Effect of Metaborate for High-Power and Long-Life Supercapacitor Electrodes. *Nano Lett.* **2017**, *17*, 429−436.
(27) Grey, C. P.; Tarascon, J. M. Sustainability and *In-situ* Monitoring in Battery Development. *Nat. Mater.* **2017**, *16*, 45−56.
(28) Li, C.; Balamurugan, J.; Kim, N. H.; Lee, J. H. Hierarchical Zn−Co−S Nanowires as Advanced Electrodes for All-Solid-State Asymmetric Supercapacitors. *Adv. Energy Mater.* **2017**, 1702014.
(29) Liu, B.; Liu, B.; Wang, Q.; Wang, X.; Xiang, Q.; Chen, D.; Shen, G. New Energy Storage Option: toward $ZnCo_2O_4$ Nanorods/Nickel Foam Architectures for High-Performance Supercapacitors. *ACS Appl. Mater. Interfaces* **2013**, *5*, 10011−10017.
(30) Zou, X.; Goswami, A.; Asefa, T. Efficient Noble Metal-Free (Electro)Catalysis of Water and Alcohol Oxidations by Zinc-Cobalt Layered Double Hydroxide. *J. Am. Chem. Soc.* **2013**, *135*, 17242−17245.
(31) Qiao, C.; Zhang, Y.; Zhu, Y.; Cao, C.; Bao, X.; Xu, J. One-Step Synthesis of Zinc−Cobalt Layered Double Hydroxide (Zn−Co-LDH) Nanosheets for High-Efficiency Oxygen Evolution Reaction. *J. Mater. Chem. A* **2015**, *3*, 6878−6883.
(32) Woo, M. A.; Song, M.; Kim, T. W.; Kim, I. Y.; Ju, J.; Lee, Y. S.; Kim, S. J.; Choy, J.; Hwang, S. Mixed Valence Zn−Co-Layered Double Hydroxides and Their Exfoliated Nanosheets with Electrode Functionality. *J. Mater. Chem.* **2011**, *21*, 4286−4292.
(33) Chen, H.; Hu, L. F.; Chen, M.; Yan, Y.; Wu, L. M. Nickel−Cobalt Layered Double Hydroxide Nanosheets for High-Performance Supercapacitor Electrode Materials. *Adv. Funct. Mater.* **2014**, *24*, 934−942.
(34) Jiang, Y.; Song, Y.; Li, Y.; Tian, W.; Pan, Z.; Yang, P.; Li, Y.; Gu, Q.; Hu, L. Charge Transfer in Ultrafine LDH Nanosheets/Graphene Interface with Superior Capacitive Energy Storage Performance. *ACS Appl. Mater. Interfaces* **2017**, *9*, 37645−37654.
(35) Arabi, M.; Ostovan, A.; Ghaedi, M.; Purkait, M. K. Novel Strategy for Synthesis of Magnetic Dummy Molecularly Imprinted Nanoparticles Based on Functionalized Silica as An Efficient Sorbent for the Determination of Acrylamide in Potato Chips: Optimization by Experimental Design Methodology. *Talanta* **2016**, *154*, 526−532.
(36) Geng, F. X.; Xin, H.; Matsushita, Y.; Ma, R. Z.; Tanaka, M.; Izumi, F.; Iyi, N.; Sasaki, T. New Layered Rare-Earth Hydroxides with Anion-Exchange Properties. *Chem. - Eur. J.* **2008**, *14*, 9255−9260.
(37) Ma, R.; Liu, Z.; Li, L.; Iyi, N.; Sasaki, T. Exfoliating Layered Double Hydroxides in Formamide: A Method to Obtain Positively Charged Nanosheets. *J. Mater. Chem.* **2006**, *16*, 3809−3813.
(38) Wang, J.; Tan, C. F.; Zhu, T.; Ho, G. W. Topotactic Consolidation of Monocrystalline CoZn Hydroxides for Advanced Oxygen Evolution Electrodes. *Angew. Chem., Int. Ed.* **2016**, *55*, 10326−10330.
(39) Hu, B.; Chen, S. F.; Liu, S. J.; Wu, Q. S.; Yao, W. T.; Yu, S. H. Controllable Synthesis of Zinc-Substituted α-and β-Nickel Hydroxide Nanostructures and Their Collective Intrinsic Properties. *Chem. - Eur. J.* **2008**, *14*, 8928−38.
(40) Patro, P. K.; Kulkarni, A. R.; Harendranath, C. S. Combustion Synthesis of $Sr_{0.5}Ba_{0.5}Nb_2O_6$ and Effect of Fuel on Its Microstructure and Dielectric Properties. *Mater. Res. Bull.* **2003**, *38*, 249−259.
(41) Jiang, S.; Pang, M.; Zhao, J.; Xing, B.; Pan, Q.; Yang, H.; Qu, W.; Gu, L.; Wang, H. Superior Performance Asymmetric Supercapacitors Based on A Directly Grown Three-Dimensional Lawn-like Cobalt-Zinc Hydroxyfluorides Nanoneedle Arrays Electrode. *Chem. Eng. J.* **2017**, *326*, 1048−1057.
(42) Cai, D.; Huang, H.; Wang, D.; Liu, B.; Wang, L.; Liu, Y.; Li, Q.; Wang, T. High-Performance Supercapacitor Electrode Based on the Unique ZnO@ Co_3O_4 Core/Shell Heterostructures on Nickel Foam. *ACS Appl. Mater. Interfaces* **2014**, *6*, 15905−15912.
(43) He, Y. M.; Chen, W. J.; Li, X. D.; Zhang, Z. X.; Fu, J. C.; Zhao, C. H.; Xie, E. Q. Freestanding Three-Dimensional Graphene/MnO_2 Composite Networks as Ultralight and Flexible Supercapacitor Electrodes. *ACS Nano* **2013**, *7*, 174−182.
(44) Gupta, V.; Gupta, S.; Miura, N. Statically Deposited Nanostructured Co_xNi_{1-x} Layered Double Hydroxides as Electrode Materials for Redox-Supercapacitors. *J. Power Sources* **2008**, *175*, 680−685.
(45) Xu, J.; Gai, S.; He, F.; Niu, N.; Gao, P.; Chen, Y.; Yang, P. Reduced Graphene Oxide/Ni1-xCoxAl-Layered Double Hydroxide Composites: Preparation and High Supercapacitor Performance. *Dalton Trans.* **2014**, *43*, 11667−11675.
(46) Wu, X.; Jiang, L.; Long, C.; Wei, T.; Fan, Z. Dual Support System Ensuring Porous Co-Al Hydroxide Nanosheets with Ultrahigh Rate Performance and High Energy Density for Supercapacitors. *Adv. Funct. Mater.* **2015**, *25*, 1648−1655.
(47) Venkatachalam, V.; Alsalme, A.; Alswieleh, A.; Jayavel, R. Double Hydroxide Mediated Synthesis of Nanostructured $ZnCo_2O_4$ as High-performance Electrode Material for Supercapacitor Applications. *Chem. Eng. J.* **2017**, *321*, 474−483.
(48) Wu, N.; Low, J.; Liu, T.; Yu, J.; Cao, S. Hierarchical Hollow Cages of Mn-Co Layered Double Hydroxide as Supercapacitor Electrode Materials. *Appl. Surf. Sci.* **2017**, *413*, 35−40.
(49) Yuan, C.; Yang, L.; Hou, L.; Shen, L.; Zhang, X.; Lou, X. W. Growth of Ultrathin Mesoporous Co_3O_4 Nanosheet Arrays on Ni Foam for High-Performance Electrochemical Capacitors. *Energy Environ. Sci.* **2012**, *5*, 7883−7887.
(50) Wang, L.; Lin, C.; Zhang, F.; Jin, J. Phase Transformation Guided Single Layer β-$Co(OH)_2$ Nanosheets for Pseudocapacitive Electrodes. *ACS Nano* **2014**, *8*, 3724−3724.
(51) Wang, Y.; Zhong, Z.; Chen, Y.; Ng, C. T.; Lin, J. Controllable Synthesis of Co_3O_4 from Nanosize to Microsize with Large-scale Exposure of Active Crystal Planes and Their Excellent Rate Capability in Supercapacitors Based on the Crystal Plane Effect. *Nano Res.* **2011**, *4*, 695.
(52) Wang, L.; Dong, Z. H.; Wang, Z. G.; Zhang, F. X.; Jin, J. Layered α-$Co(OH)_2$ Nanocones as Electrode Materials for Pseudocapacitors: Understanding the Effect of Interlayer Space on Electrochemical Activity. *Adv. Funct. Mater.* **2013**, *23*, 2758−2764.
(53) Zhi, M.; Xiang, C.; Li, J.; Li, M.; Wu, N. Nanostructured Carbon−Metal Oxide Composite Electrodes for Supercapacitors: A Review. *Nanoscale* **2013**, *5*, 72−88.
(54) Fan, H.; Niu, R.; Duan, J.; Liu, W.; Shen, W. Fe_3O_4@ Carbon Nanosheets for All-Solid-State Supercapacitor Electrodes. *ACS Appl. Mater. Interfaces* **2016**, *8*, 19475−19483.
(55) Yu, N.; Yin, H.; Zhang, W.; Liu, Y.; Tang, Z. Y.; Zhu, M. Q. High-Performance Fiber-Shaped All-Solid-State Asymmetric Super-

DOI: 10.1021/acsnano.8b00653
ACS Nano 2018, 12, 2968−2979

capacitors Based on Ultrathin MnO_2 Nanosheet/Carbon Fiber Cathodes for Wearable Electronics. *Adv. Energy Mater.* **2016**, *6*, 1501458.
(56) Kim, M.; Yoo, J.; Kim, J. Quasi-Solid-State Flexible Asymmetric Supercapacitor Based on Ferroferric Oxide Nanoparticles on Porous Silicon Carbide with Redox-active p-Nitroaniline Gel Electrolyte. *Chem. Eng. J.* **2017**, *324*, 93−103.
(57) Liu, Q.; Wang, B.; Chen, J.; Li, F.; Liu, K.; Wang, Y.; Li, M.; Lu, Z.; Wang, W.; Wang, D. Facile Synthesis of Three-Dimensional (3D) Interconnecting Polypyrrole (PPy) Nanowires/Nanofibrous Textile Composite Electrode for High Performance Supercapacitors. *Composites, Part A* **2017**, *101*, 30−40.
(58) Chen, J.; Wei, H. M.; Fu, N.; Chen, H. J.; Lan, G. X.; Lin, H. L.; Han, S. Facile Synthesis of Nitrogen-Containing Porous Carbon as Electrode Materials for Superior-Performance Electrical Double-Layer Capacitors. *J. Mater. Sci.* **2018**, *53*, 2137−2148.
(59) Zhai, T.; Lu, X.; Wang, H.; Wang, G.; Mathis, T.; Liu, T.; Li, C.; Tong, Y.; Li, Y. An Electrochemical Capacitor with Applicable Energy Density of 7.4 Wh/kg at Average Power Density of 3000 W/kg. *Nano Lett.* **2015**, *15*, 3189−3194.
(60) Chen, Z.; Augustyn, V.; Wen, J.; Zhang, Y.; Shen, M.; Dunn, B.; Lu, Y. High-Performance Supercapacitors Based on Intertwined CNT/V_2O_5 Nanowire Nanocomposites. *Adv. Mater.* **2011**, *23*, 791−795.
(61) Zhao, R.; Wang, M.; Zhao, D.; Li, H.; Wang, C.; Yin, L. Molecular-Level Heterostructures Assembled from Titanium Carbide MXene and Ni-Co-Al Layered Double Hydroxide Nanosheets for All-Solid-State Flexible Asymmetric High-Energy Supercapacitors. *ACS Energy Lett.* **2018**, *3*, 132−140.
(62) Wang, H.; Gao, Q.; Hu, J. Asymmetric Capacitor Based on Superior Porous Ni−Zn−Co Oxide/Hydroxide and Carbon Electrodes. *J. Power Sources* **2010**, *195*, 3017−3024.
(63) Guan, B.; Guo, D.; Hu, L.; Zhang, G.; Fu, T.; Ren, W.; Li, J.; Li, Q. Facile Synthesis of $ZnCo_2O_4$ Nanowire Cluster Arrays on Ni Foam for High-Performance Asymmetric Supercapacitors. *J. Mater. Chem. A* **2014**, *2*, 16116−16123.
(64) Wu, C.; Cai, J.; Zhang, Q.; Zhou, X.; Zhu, Y.; Shen, P. K.; Zhang, K. Hierarchical Mesoporous Zinc−nickel−cobalt Ternary Oxide Nanowire Arrays on Nickel Foam as High-Performance Electrodes for Supercapacitors. *ACS Appl. Mater. Interfaces* **2015**, *7*, 26512−26521.
(65) Zhao, Y.; Ma, H.; Huang, S.; Zhang, X.; Xia, M.; Tang, Y.; Ma, Z. Monolayer Nickel Cobalt Hydroxyl Carbonate for High Performance All-solid-state Asymmetric Supercapacitors. *ACS Appl. Mater. Interfaces* **2016**, *8*, 22997−23005.

DOI: 10.1021/acsnano.8b00653
ACS Nano 2018, 12, 2968−2979